IOP Publishing Journal of Physics D: Applied Physics

J. Phys. D: Appl. Phys. **49** (2016) 015202 (10pp) doi:10.1088/0022-3727/49/1/015202

# Structure of propagating arc in a magneto-hydrodynamic rail plasma actuator

**Miles D Gray, Young-Joon Choi, Jayant Sirohi and Laxminarayan L Raja**

Department of Aerospace Engineering and Engineering Mechanics, The University of Texas at Austin, Austin, Texas 78712, USA

E-mail: miles.gray@utexas.edu

Received 20 July 2015, revised 12 October 2015
Accepted for publication 19 October 2015
Published 18 November 2015


**Abstract**

The spatio-temporal evolution of a magnetically driven arc in a rail plasma flow actuator has been characterized with high-speed imaging, electrical measurements, and spectroscopy. The arc draws a peak current of ~1 kA. High-speed framing cameras were used to observe the complex arc propagation phenomenon. In particular, the anode and cathode roots were observed to have different modes of transit, which resulted in distinct types of electrode degradation on the anode and cathode surfaces. Observations of the arc electrical properties and induced magnetic fields are used to explain the transit mechanism of the arc. Emission spectroscopy revealed the arc temperature and species composition as a function of transit distance of the arc. The results obtained offer significant insights into the electromagnetic properties of the arc-rail system as well as arc-surface interaction phenomena in a propagating arc.

Keywords: flow actuation, plasma, spectroscopy, atmospheric pressure, arc, magnetohydrodynamic, railPAc

(Some figures may appear in colour only in the online journal)

## 1. Introduction

Magnetically driven arcs are encountered in a variety of engineering applications, including as chemical reactors for gas stream processing [1], arc flow control devices [2], plasma armature railguns [3], and circuit breakers [4]. The arcs generated in these devices move over extended electrode surfaces through Lorentz forcing resulting from interaction between the naturally induced magnetic field and the electrical current passing through the arc.

Study of the structure and motion of magnetically driven arcs illustrates a rich variety of features. For example, the arc maintains a 'single arc mode' with a single coherent arc column at low currents, but can transition to a 'distributed arc mode' at high currents, especially if the arc is confined within close gap dielectric walls. In this distributed arc mode, multiple arc columns form simultaneously as a result of restrike phenomena, where hot gas and ablated wall or electrode material in the vicinity of a primary moving arc column alter conditions enough to produce an additional local breakdown [5, 6]. Other arc motion modes may be characterized by whether arc roots move smoothly over the electrode surface or in distinct jumps with 'anchored' pauses [7].

When driven magnetically, the forward movement of the arc is facilitated by a distortion of the arc column in the direction of the Lorentz forces. As the column is pushed forward by the Lorentz force, the arc roots are either dragged along behind, or the column forms a new root ahead of the old roots [4, 8]. Arc roots tend to propagate by a discontinuous motion on the anode side, switching between moving and anchored modes, but tend to stay in a smooth continuous movement mode on the cathode side [9, 10]. The anchoring of the arc has been shown to be a strong function of electrode material, with more easily evaporated materials producing longer anchoring times [11]. These modes also play a major role on damage imparted to the electrode surface, with crater/spot damage on the electrode surface at the location where the arc root anchors to the surface [10].

The arc-heating of the gas produces large dilatational (volumetric expansion) effects that can have an impact on the arc structure and its motion [12–14]. For example, natural convection effects can be destabilizing for an arc and cause arc

 

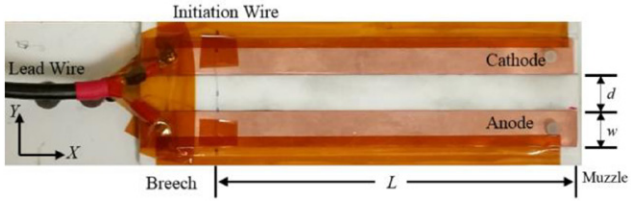


**Figure 1.** A top view of the experimental RailPAc prototype. The arc propagates along the *X* direction. The *Z*-axis is oriented out of the page. The rails here are separated by a distance (d) of 13 mm, and are each 13 mm wide (w), and 152 mm long. The distance from initiation point (breech) to muzzle (*L*) is 127 mm.

column motion. Hot expanding gases can also push the arc away from the wall surface, distorting the column structure [4].

Recently, our group proposed a novel atmospheric pressure aerodynamic plasma flow actuator device capable of large induced flow velocities of ~10's m $s^{-1}$ [2] using a magnetically driven arc discharge. The device (called a Rail Plasma Actuator or 'RailPAc') uses extended rail electrodes over which the arc is set in motion through Lorentz forcing, which in turn induces flow in the surrounding air. The structure and dynamics of arc motion in the RailPAc device is the subject of this study.

## 2. Experimental setup

The experimental setup for the study of driven arc phenomena in an experimental RailPAc device is shown in figure 1. RailPAc operation was described in detail in our previous paper [2]. A summary of the RailPAc operation is presented below.

To begin, an arc is initiated at one end (the breech end shown in figure 1) of a pair of parallel long flat electrodes (rails) that are mounted on a dieletric surface. The arc is powered by a pulse forming network (PFN) connected at the breech end of one of the rails. The other rail is grounded, also at the breech end. A current loop is formed by its path through the lead wire into the powered rail, across the arc to the ground rail, and then out through the other lead wire. This current loop induces a magnetic field in the plane perpendicular to the rail electrodes. The sense of this field is such that the Lorentz ($J \times B$) force acting on the arc column pushes the arc along the length of the rails in the direction opposite to the connection with the PFN. While the principle of Lorentz forcing is common to all magnetically driven arcs, the novelty of the RailPAc device is its use of the arc motion to induce velocity in the surrounding air, resulting in an effective low-speed, atmospheric pressure aerodynamic flow actuator [2].

In the experiments discussed in this paper, the rails are made of copper and measure 152 mm long, 13 mm wide, and 0.6 mm thick. The thickness of the electrodes has limited effect on the transit of the arc since only the top surface of the electrode is exposed to air. The thickness used here was chosen to minize the invasion into any structure on which the RailPAc is mounted while also maintaining low electrical resistance and mitigating flexure due to Lorentz forcing. The electrodes are flush mounted on a Macor ceramic plate and are spaced

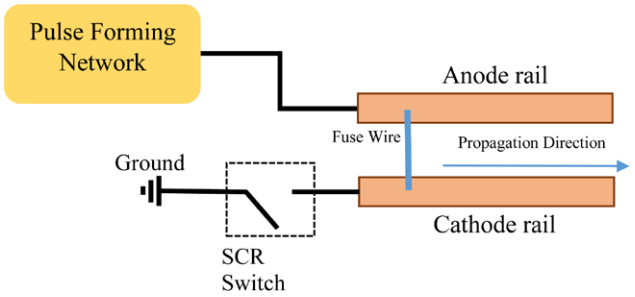


**Figure 2.** A schematic of the RailPAc experimental system. The pulse forming network brings both the anode and cathode rails to positive potential and then the SCR switch drops the cathode rail to ground. This draws current through the fuse wire, which explodes, forming the arc which then propogates down the rails until the pulse forming network ceases current supply.

13 mm apart. The arc is initiated with an aluminum-copper alloy fuse wire placed 25 mm from the breech end of the rails. The location of the initiation wire and the rail length limits the maximum transit distance (*L*) to 127 mm. Following railgun convention, this paper will refer to the lead wire attachment side of the rails as the 'breech', and the opposite end of the rails as the 'muzzle' [21]. A fuse wire was used for initiation purposes to maximize reproducibility since the high voltage initiation used in [2] does not always initiate the arc in the same place on the rails.

The RailPAc prototype was powered by the pulse forming network indicated in figure 2. The network consists of a capacitor bank, inductor, and a silicon controlled rectifier (SCR), and provides a ~5 ms half pulse of current based on the *LC* time constant of the network. The capacitor bank is comprised of six electrolytic capacitors (Sprague Powerlytic 36DX) set up in parallel with a total capacitance of 21 mF. The bank is charged with a Xantrex XHR 600 DC power supply and discharged when a trigger voltage is supplied to the SCR. After the trigger voltage is applied, a large current from the capacitor vaporizes the fuse wire and subsequently forms an electrical arc across the rails.

### 2.1. Electrical measurements

Electrical measurements were conducted to determine the transient arc current *I*, capacitor bank voltage $V_{cap}$, and breech voltage $V_{breech}$ during the arc transit. The arc current was measured with a Rogowski coil on the ground side of the SCR by numerically integrating its signal in time. A P5205 differential voltage probe was connected to the lead wire attachment points at the breech end of the rails to measure breech voltage, and another was attached to the capacitor bank terminals to monitor the capacitor bank voltage. The signals from each measurement device were acquired with Tektronix TDS 3014B oscilloscopes at a sampling frequency of 500 kHz.

### 2.2. High-speed imaging

Three high-speed cameras were placed along three mutually orthogonal directions to characterize the arc shape in three

**Table 1.** High-speed camera specifications and viewing orientations.

| Camera | Viewing direction | Frame rate (per second) | Resolution (pixels) | Mylar filter | Exposure time ($\mu$s) | Sensitivity (ISO) |
|---|---|---|---|---|---|---|
| Phantom Miro M-310 | $-x$ | 26000 | 320 × 240 | Yes | 10 | 3900 |
| Phantom Miro M-310 | $-y$ | 13000 | 512 × 320 | Yes | 1 | 3900 |
| Phantom V5 | $-z$ | 13000 | 256 × 256 | No | 2 | 600 |

dimensions. A Phantom V5 camera was mounted above the RailPAc prototype to capture the transit event from above. Two Phantom Miro M-310 cameras were mounted on the anode side and muzzle side to capture the side view and frontal view of the arc, respectively. The Miro M-310 series cameras have higher sensitivity CCD arrays than the V5, with an ISO of 3900 in the Miro M-310 compared to an ISO of 600 in the V5, so a thin Mylar film (10 mil) was used as a filter for the two Miro cameras. Table 1 lists the frame rates, resolutions, and filters used in the high-speed imaging. All lenses used an F-stop of 22 for all acquisitions. Differences in frame rate between the two M-310 cameras are due to the relative size of each camera's target which called for different resolutions. The phantom V5 has a lower maximum framerate than the M-310.

### 2.3. Spectroscopy

An Ocean Optics HR2000 + spectrometer was used to measure temperature and species composition of the arc. The spectrometer has a resolution of 0.065 nm with responsive range of 200–1100 nm. However, the tungsten calibration source used to calibrate the spectrometer and the fiber optic cable used in the light collection system reduced the reliable spectral response to a range of about 400–900 nm. A collimating tube was used to limit the spectrometer field of view. This tube has a small viewing port on each end that limits the viewing angle (hard angle) of the spectrometer to 1.1°. The spectrometer was connected to the collimating tube with a 400 $\mu$m fiber-optic cable. Measurements were taken from approximately 15 cm away from the RailPAc surface at a 45° angle up from the plane of the rails, resulting in an elliptical field of view with a minor axis length ~1.5 mm and a major axis length ~2.0 mm. This small field of view provides a simple means of resolving the behavior of the arc in time and space as it transits along the rails. The collimating tube was moved down the rails in increments of 1.3 cm to track changes in the arc's behavior during its transit down the rail. Data was taken at each increment by integrating all incident light on the spectrometer for 10 ms after initiation of the arc. As a result, the absolute intensity of light emitted by the arc cannot be determined.

Several techniques were used to analyze the accumulated spectral data. Analysis of measured data and comparison with values for known strong emission lines from NIST [15] and Camacho's analysis of nitrogen plasmas [16] allowed determination of species present in the arc. By integrating the area under emission lines of one species and comparing them with the integrated area under lines of another species, the evolution of species ratios as the arc propagates along the rails can be estimated, provided that temperature does not vary significantly between measurements. Temperature was measured by assuming that the majority of light emitted by the arc comes from the core of the plasma column, which is assumed to be in local thermodynamic equilibrium (LTE) and that self-absorption by the plasma column is negligible. The condition of LTE implies that

$$n_i = \frac{ng_i}{Z}\exp\left(\frac{-E_i}{k_B T}\right) \tag{1}$$

where $n_i$ is the density of a state, $n$ is total density of the species, $g_i$ is the degeneracy of the state, $Z$ is the partition function of the system, $T$ is the temperature, $E_i$ is the energy of the state, and $k_B$ is Boltzmann's constant. The absolute emission intensity per unit solid angle $I_{ij}$ of a spectral line resulting from transition from state $i$ to state $j$ is given by

$$I_{ij} = \frac{V}{4\pi} A_{ij}\, n_i\, h\nu_{ij} \tag{2}$$

where, $V$ is the volume from which light is emitted, $A_{ij}$ is the Einstein emission coefficient for the spectral line, and $h\nu_{ij}$ is the energy of the photon. Rearranging equations (1) and (2), one can obtain the relation

$$\ln\left(\frac{I_{ij}}{g_i A_{ij} h\nu_{ij}}\right) = \ln\left(\frac{Vn}{4\pi Z}\right) - \frac{E_i}{k_B T} \tag{3}$$

Since all of the quantities in the first term on the right-hand side are constant for a given spectra, the slope of the line created by the quantity on the left-hand side plotted relative to the energy of the upper state of the emitting species, $E_i$, gives the temperature. This method is typically referred to as the 'Boltzmann plot approach' to determining temperature [17]. Since Boltzmann plots only allow as many data points for each measurement as there are spectral lines with well-known emission parameters, this technique was further refined by normalizing the left-hand side of equation (3) to zero for one of the spectral lines and only looking at the relative position of the other lines in the Boltzmann plot space to calculate the regression line that yields the temperature. This allowed for the inclusion of data from several runs in the same Boltzmann plot, drastically increasing the accuracy of the temperature measurements.

## 3. Results and discussion

Electrical characteristics of the arc are discussed first. Electrical data was taken for ~100 firings and data froms each of these was synthesized to find consistent trends in the highly non-repeatable process of the gliding arc. Data

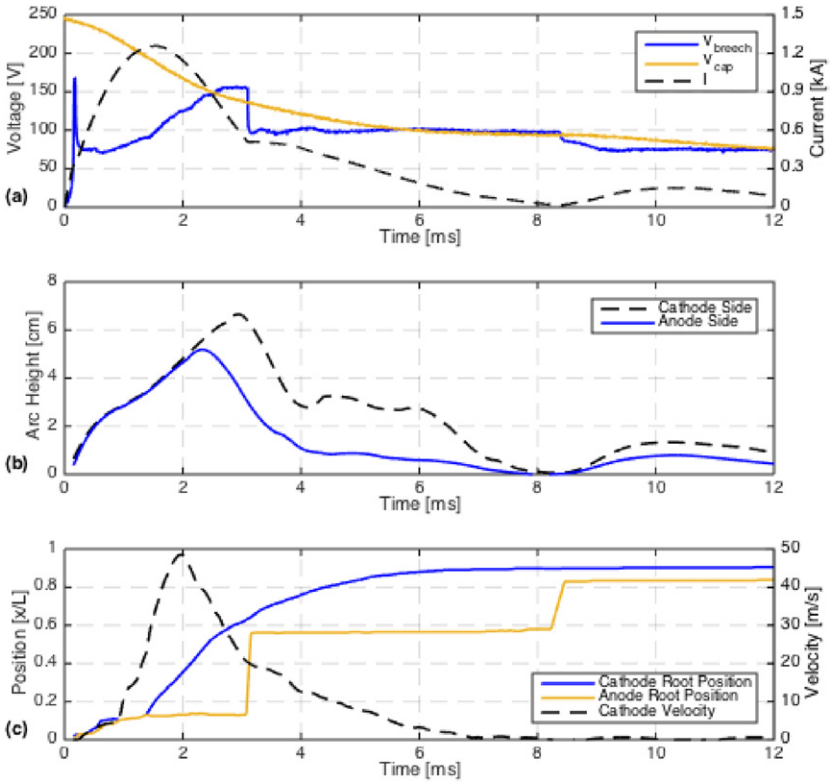


**Figure 3.** (a) Electrical characteristics of the arc, (b) Discharge column height, and (c) Arc root positions and cathode root velocity. Notice that the peak current in (a) occurs during the strong initial acceleration of the arc and precedes the peak velocity in (c). The connections between the anode root jump at 3 ms in (c) and the breech voltage drop in (a) is clearly visible here.

from a single representative firing which displays many of the consistently observed characteristics of a RailPAc firing is presented in figure 3. The capacitor bank was charged to an initial voltage of 250 V, which corresponds to a stored energy of 656 J. Figure 3(a) shows the transients for the arc current $I$, capacitor bank voltage $V_{\text{cap}}$, and breech voltage $V_{\text{breech}}$. The capacitor voltage discharges from 250 V to approximately 80 V at the end of the transient, corresponding to a total energy of 580 J delivered to combination of the discharge and the resistive load of the circuit. The energy delivered to the discharge alone may be calculated by the relationship,

$$E_{\text{discharge}} = \int V_{\text{breech}} I^2 \mathrm{d}t \tag{4}$$

$E_{\text{discharge}}$ was found to be ~350 J of the 580 J delivered to the whole circuit. The overall discharge time was found to be ~19 ms, which is significantly longer than the 5 ms half-cycle time of the pulse forming network. The current waveform in figure 3(a) also indicates that the discharge follows the response of a typical RLC circuit until 3 ms, when a discontinuity in the current slope and breech voltage occurs. These discontinuities at $t \sim 3$ ms and $t \sim 8.5$ ms prolong the discharge time by decreasing the rate of decay of the current draw. Previous studies have shown that such rapid drops in voltage correspond to jumps in the anode arc root location and associated erosion of the anode material [7, 10]. Both claims have been confirmed here by correlating the anode erosion damage locations on the rails with the locations of anode root anchoring in the high-speed images.

The behavior of the transient arc can be observed from the high-speed images in figure 4, which show the motion of the luminous arc along the rails. The intensity of the arc is strongest near the arc roots and less bright at points in the arc further away from the surface. The arc column appears as a luminescent cloud that diffuses throughout the current-path of the arc. Unfortunately, it is difficult to distinguish the part of this luminous cloud that is current-carrying ionized plasma from the part that is strongly radiating non-ionized gas. Parker [3] has shown that in railgun applications a significant portion of the luminous cloud is non-ionized or weakly-ionized and does not carry significant current across the electrodes. Imaging of the luminous cloud is therefore not a definite measure of the location of the current-carrying arc, so the location of the cloud can only be used as a bound for the outer edge of the arc column.

The arc column height, $h$, arc root positions, $x$, and propagation velocity, $u$, were interpreted from the high-speed images shown in figure 4. These results are shown in figure 3(b) and (c). Due to the discontinuous jumps in the anode root motion, the cathode root motion was used to approximate the propagation velocity of the arc. Closer analysis reveals that several of the observed arc characteristics are consistent with the measured current, particularly the acceleration of the arc which shares its peak with the maximum current of the discharge. This is an expected result given that the Lorentz force is proportional to the square of the current. The local arc velocity,

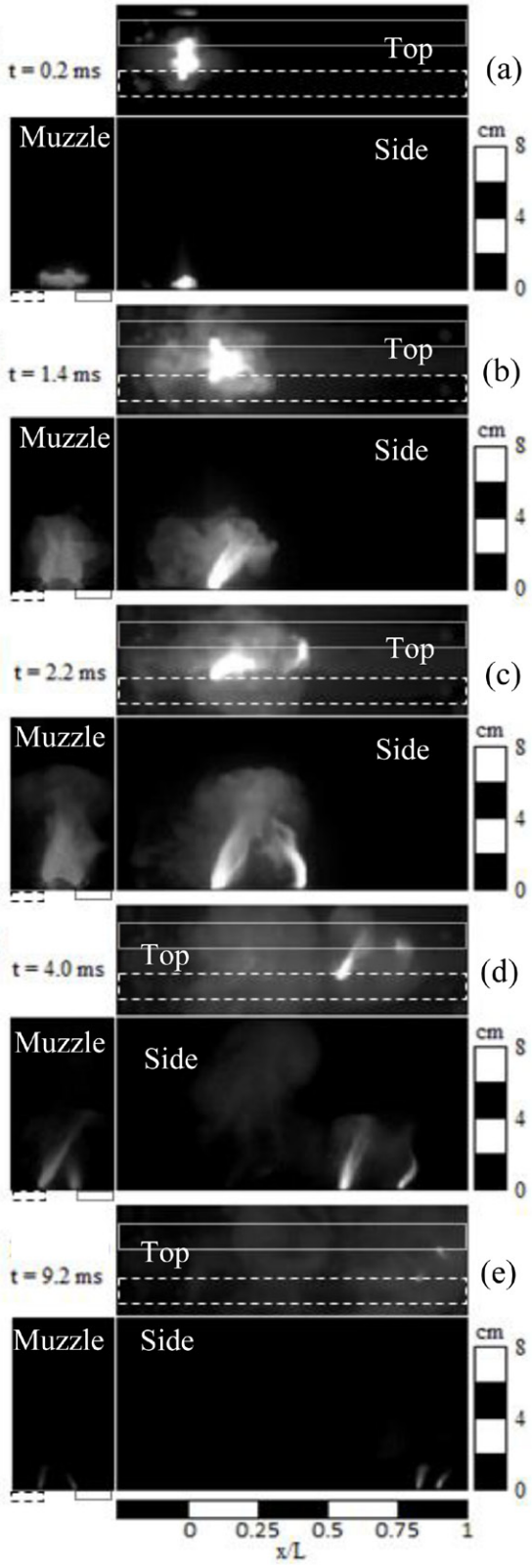


**Figure 4.** High-speed images of the arc transit. Each subfigure shows the top, side, and muzzle view of the propogating arc at a single time. Scales showing the height above the rail surface and the normalized distance traveled are shown at the sides of each image. The dashed lines mark the location of the anode while the solid lines mark the location of the cathode. The initiation stage spans (a) and (b), the main transit stage occurs in (c) and (d), while the quenching stage occurs in (e).

which depends on the arc acceleration, is also (indirectly) affected by the arc's current.

The arc height and the breech voltage of the arc are also related to one another. The maximum height of the discharge increases as the voltage increases and then begins to fall immediately after the first drop in breech voltage shown in figures 3(a) and (b) at around 3 ms.

The arc's transit may be classified into three stages based on the geometric and electrical properties of the arc. The initiation stage corresponds to the ignition of the arc at the time of the trigger and the transit duration around 1 ms after the trigger. It can be characterized by the acceleration of a coherent arc column. In this stage, the breech voltage initially spikes and then remains relatively steady or increases marginally (by no more than ~20 V), while the current rapidly increases. The main transit stage is marked by a smooth transit of the cathode root and discontinuous jumps of the anode root. The jumps cause fluctuations in the breech voltage and current throughout the main transit stage. The end of the transit shows quenching of the arc, as evidenced by reduction in arc intensity and current.

### *3.1. Initiation stage*

The breech voltage in figure 3(a) contains a large initial peak at $t \sim 0.1$ ms corresponding to the vaporization of the initiation wire. After this peak, the breech voltage drops to ~80 V and then gradually increases during the initiation stage. The images in figure 4 show the formation of a single coherent arc column between the electrodes at $t \sim 0.2$ ms. This arc column immediately experiences a large acceleration along the rails due to the Lorentz force. During the initial transit, the anode and cathode arc roots propagate as a single column. The initiation stage is specifically defined by the period where the roots form and then propagate together in this concerted fashion. This concerted propagation can be seen in the image at $t \sim 1.4$ ms in figure 4. The arc column grows in height (figure 3(b)) with increasing arc current and forms an arch-like shape above the surface.

The deflection of the arc away from the surface, evident in figure 4, can be explained by geometric factors and the consequent electromagnetic forces. Figure 5 presents a schematic of the arc structure and the forces acting on the arc for a symmetric case where there is no insulating surface between the electrodes, as well as for a case like RailPAc with an insulating surface and flush-mounted electrodes. The presence of the insulating surface creates an initial distortion of the arc column into the open air, but this distortion is immediately magnified by the same self-blowing effect that pushes the arc down the rails. When the arc is in plane with all current localized between the electrodes, the only force on the arc is the forward Lorentz force in the same direction as the electrode length. However, if the arc is displaced such that some current comes out of plane, the magnetic field in the area of the plasma develops a component which points towards the breech. The arc current then interacts with this field, resulting in an expansion of the arc upward and outward. Due to the field enhancement at the edges of the rail electrodes, the arc roots are not

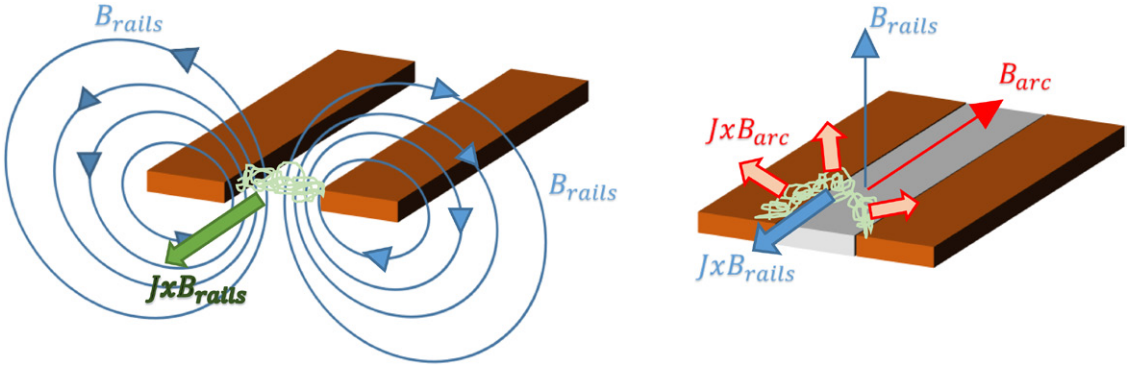


**Figure 5.** The arc on the left is allowed to stay between the electrodes and thus has no force component in the vertical direction. The arc on the right has been forced out of the plane by the surface between the rails. In this case, the arc induces its own magnetic field, $B_{arc}$, parallel to the rails and orthogonal to the field induced by the current passing through the rails. This causes a Lorentz force on the arc perpendicular to the surface, pushing it upward and outward.

always noticeably affected by this force. However, the plasma column always rises upward as the current reaches peak values and enters into the main transit stage. It is likely that this effect is aided by the gas expansion effects described in [4, 12], and [14]. The arc heats the gas around it, causing the gas to expand and push the arc away from the surface.

### 3.2. Main transit stage

The main transit stage begins after about 2 ms as shown in figure 4. The arc current reaches a peak value of 1.3 kA at around 2 ms and the arc velocity reaches a peak value of ~50 m $s^{-1}$ during the later part of the transit at around 5 ms. The single coherent arc observed in the initiation stage is transformed to a diffuse column between the electrodes. This column cannot be observed at all instances because of the surrounding luminous cloud, however, the cathode and anode arc roots regions are clearly visible throughout the transit.

The discharge columns extends away from the surface until the first sharp drop in breech voltage at around 3 ms, after which point the columns begin to decrease in height. As shown in figure 3(b), the cloud extends almost 7 cm away from the surface at its peak height. This suggests that a large region of surrounding quiescent air is affected by the arc transit, i.e. the flow actuation effect can extend several centimeters away from the surface (a desirable feature for surface plasma actuators). The height of the arc above each electrode is independently estimated by finding the cloud height at the respective locations of the arc roots. It can be seen in figure 4(d) that the anode side of the arc column has higher intensity and height than the cathode side of the arc column.

During the main transit stage, the cathode root moves smoothly along the cathode, while the anode root periodically anchors on the anode surface and then jumps forward to catch up to the cathode root. The motion of the anode root is punctuated by the formation of a new anode root directly across from the cathode root whenever the distance between the arc roots is increased. Indeed, the arc column splits to allow the existence of two anode roots to appear simultaneously with the 2 $\mu$s exposure time of the camera used. As the new anode root forms, the original anode root is extinguished. The time

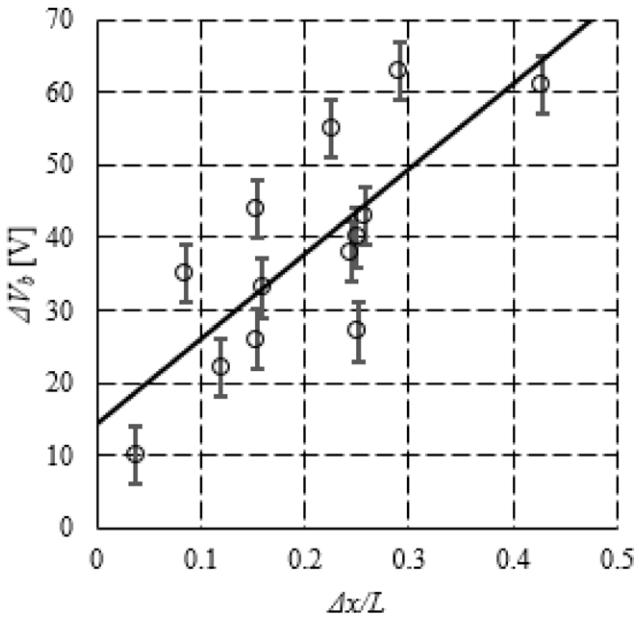


**Figure 6.** Breech voltage drop as a function of arc root jump distance.

and location of this process is not consistent from one firing to another. However, the arc current and breech voltage measurements show consistent trends with regards to the formation and destruction of the anode roots.

The anode root jump occurs consistently after the peak arc current during the decreasing phase of the current. Before the jump, the distance between the anode and cathode roots increases because the anode root is anchored to the electrode while the cathode root continues to move forward smoothly. As the roots move further apart the arc must necessarily lengthen, which increases the electrical resistance of the arc. This increase in the arc's electrical resistance works to decrease the current passing through the circuit, however, the circuit's inductance minimizes this change in current by generating an inductive EMF to match the rise in resistance. This electromotive force from the circuit inductance serves to directly maintain the arc current at constant values on timescales less than the natural frequency of the RLC circuit.


**Figure 7.** Comparison of electrode topologies after the first firing (top) and the fifth firing (bottom). Notice the continuous damage on the cathode side and the spot damage on the anode side.

As a result, the breech voltage rises proportionally to the arc resistance. As the breech voltage ramps up to its threshold value, which varies from shot to shot, the anode root jumps to a new location closer to the cathode root. Following the jump, the breech voltage drops to a lower value and is nearly steady for the remainder of the discharge.

Figure 6 shows the breech voltage drop as a function of the anode arc root jump distance, over a number of firings. A clear correlation is found with the breech voltage drop increasing nearly linearly as the anode root jump distance increases. This drop in voltage is a direct consequence of a decrease in the arc resistance each time the anode root jumps. The scatter in the data is attributed to the fact that the current path distance is not neccesarily a straight line through the arc roots. As a result of the breech voltage drop, the current slope suddenly changes from negative to zero at the jump. The arc column height also drops and then re-expands upward after the jump, as shown in figure 3(b).

Arc anchoring and subsequent movement in the RailPAc seems to be analogous to models for arc movement in low voltage circuit breakers described above [4, 8]. On the cathode, the root moves by a multitude of very small jumps, which are often not discernible by camera but do seem to occur as evidenced by the small closely-spaced spots of arc damage on the cathode rail surface. While the cathode moves forward smoothly, the anode anchors for long periods of time as described in [10]. This stretches the arc column down the surface of the RailPAc and populates the area downstream from the anchored anode root with excited/ionized gas. It is believed that this gas facilitates the new arc root. Meanwhile, the increase in arc resistance due to the increasing arc length makes the current path prefer a shorter, less resistive path between the roots.

At some threshold condition, due to a combination of the effects listed above, the anode jump occurs. All of the current immediately begins passing through the new anode root, which is closer to the cathode root and allows a less resistive path. The old anode root ceases to exist as described by Haug [19]. The model described above explains the drop in height seen when the anode root makes its jump, since a lower arc column is a shorter current-path.

Anode jumping behavior does not seem to be a strong function of current in the regimes studies here, as compared to transit velocity which does scale with current as shown in [18]. However, given that the jumping behavior is not observed in the high current regimes used by railguns it may be that it is a weak function of current.

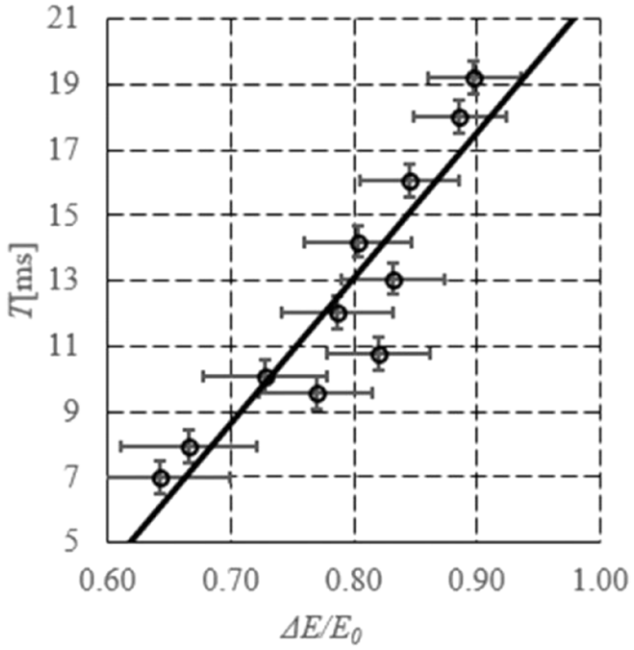


**Figure 8.** Arcing duration as a function of drops in capacitor energy normalized by the initial capacitor energy.

### 3.3. Quenching stage

The quenching stage begins when the discharge current has dropped to a sufficient small value. For low currents the Lorentz forcing is weak and the arc column ceases motion. This stage begins after 6 ms in figures 3 and in 4(e). A continuous reduction in luminosity and column height is seen during this stage. Although the root positions are fixed, the column tilts towards the muzzle end of the rails as the top of the column continues to be pushed by the weak Lorentz force. However, the roots are sufficiently anchored to resist movement. While the breech voltage is constant, the current decays to zero and the arc resistance increases until the plasma arc is completely extinguished.

In some cases, the anode root jumps once more during the quenching stage. However, the arc formation-destruction process at this stage is different from the one observed in the main transit stage. First, the cathode root does not exhibit motion before the anode jump. Second, the breech voltage does not increase prior to the jump because the arc roots are fixed and the jump occurs at a lower threshold voltage. It is clear from the comparison between the two transit stages that the increase in breech voltage is related to the increase in the relative distance between the arc roots. It appears that the reduction in current in this stage increases the time needed to reach the critical number density of charged species compared to the main transit stage.

### 3.4. Rail damage

Images of the rail electrodes after a single firing and after five firings are shown in figure 7. The arc causes substantial

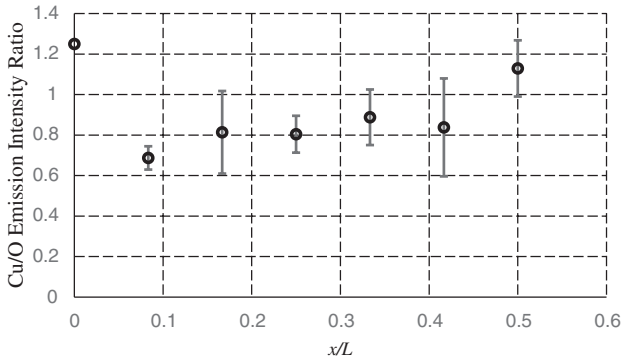


**Figure 9.** Relative ratio of visible copper emission to oxygen emission.

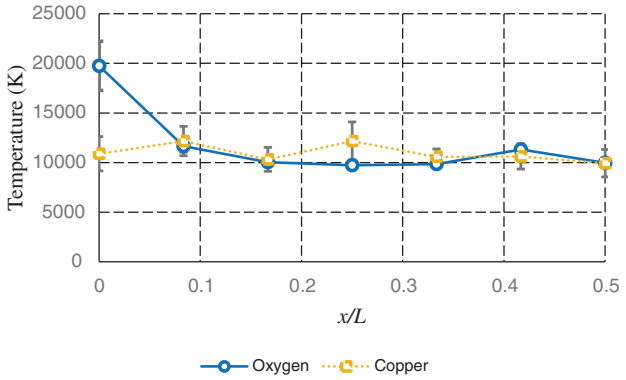


**Figure 10.** Temperature estimates of the arc using copper and oxygen species emission lines. Notice that the temperature is more or less constant after the initiation of the arc.

damage to the surface of the electrodes, concentrated around the edges of the electrodes and most intensely on the anode side. Damage on the electrodes is concentrated around the initiation region for the first few firings, but subsequent firings extend the damage towards the muzzle end. The severity of damage also increases with the number of firings.

A closer observation of the rails reveals two types of surface damage. While the cathode side is characterized by a continuous track of dark residue along the transit direction, the anode side is punctuated by anode root anchoring pits of varying shapes and sizes. Surrounding these pits are marks of copper residue left on the ceramic surface, which extend away from the rails towards the opposite electrode. The formation of anode erosion pits correspond to the anchorage of the anode roots at these positions along the rails. Copper residue is also deposited on the ceramic surface of the cathode side, however, the damage is smaller and the residue does not extend as far as the anode side. The difference is a consequence of the dwell time of the respective arc roots at any given location on the electrodes. A longer dwell time (in the case of the anode root) at a given location results in large energy transfer to the eletrodes an consequently greater erosion damage. Similar observations were made by Teste *et al* [10] in their study of arc root motion over anode and cathode surfaces.

While some quantities remain the same, there are considerable variations in arc transit characteristics from one RailPAc firing to another, and the exact characteristics of the arc transit are never fully repeatable. The peak current and peak resistance of the arc are nearly constant from one shot to the next, however, most other quantities vary considerably. The maximum velocity as well as the distance traveled by the arc before quenching are variable. The time it takes for the arc to cease discharging is also variable, as is the number of jumps that the anode root makes. Interestingly, despite the expectation that the anode spot damage locations should act as field enhancement points which may make them attractive arc root anchoring points, the number and location of jumps made seems to have no correlation with pre-existing rail damage.

The arc transit duration is found to correlate well with the energy discharged by the capacitor. Figure 8 plots the arcing duration as a function of the energy discharged by the capacitor, $\Delta E$, normalized by the initial capacitor energy ($E_0$). The minimum sustain voltage drop of the arc is relatively constant since it is largely based on the spacing of the rails. The capacitor bank can only continue to drive the arc if the bank is at a higher voltage than the minimum sustain voltage drop, so once the bank voltage drops below the sustain voltage of the arc, the arc will quench. Observation of the current and capacitor voltage waveform in figure 3(a) and of the pulse generator layout suggests that the circuit behaves like an overdamped RLC circuit. The capacitor bank energy in an ideal RLC circuit should decay exponentially as shown below,

$$\ln\left(1+\frac{\Delta E}{E_0}\right)\propto -t \tag{5}$$

The RailPAc experimental data in figure 8 shows that the capacitor bank energy decay follows the above ideal relationship.

### 3.5. Spectroscopy

Spectroscopy measurements allow for the determination of the species present in the arc during its transit. Species detected include atomic oxygen, atomic nitrogen, molecular nitrogen, atomic hydrogen, and atomic copper. Oxygen and nitrogen species are entrained directly from the surrounding air, while the presence of hydrogen is explained by breakdown of atmospheric water. Copper appears because it is present in the exploding initiation wire and is eroded from the copper rail electrodes. Oxygen, hydrogen, and copper are all strong emitters but hydrogen has only two strong lines in the region analyzed, making it a poor candidate for spectral analysis. Most of our spectral analysis thus concentrates on only oxygen and copper species.

While the exact ratio of all of the species could not be determined from simple spectral data, relative increases and decreases in the ratio of species in the arc can be estimated. This is done by comparing the total emission in the region of interest for different species at multiple points in the transit. Values were computed for the strongest emitters, oxygen and copper, and are shown in figure 9. The results suggest that there is a relatively high amount of copper present at the initiation (due to the exploding wire), and then oxygen is entrained into the arc in the first couple of centimeters of transit while

copper vapor from the exploding wire condenses on the railpac surface, which corresponds roughly to the initiation phase described previously. Most of the main transit is captured and shows a steady increase in copper relative to oxygen due to erosion of copper from the electrodes. The quench phase is not bright enough for analysis with the current setup and would require more complex analysis, since the arc is not expected to be at LTE.

Temperature estimates were obtained using the normalized Boltzmann plot method described earlier and are shown graphically in figure 10. Estimates of temperature were made using copper and oxygen. Measurements at the arc initiation ($x/L = 0$) for oxygen are not reliable because the system is likely not at LTE conditions during this time and the high density of copper vapor at this stage increase the likelihood of self-absorption of photons by the plasma column. This is also evident in figure 9, which shows that the timescales for entraining oxygen into the arc and removing the initial deposit of copper from the fuse wire are non-negligible compared to the timescales associated with the arc transit. Arc temperature appears nearly constant at about 10 000 K through the first two stages of the transit.

While self-absorption of copper is possible and could lead to incorrect estimates of temperature, self-absorption of oxygen to generate a consistent change in temperature such that both elements create an equal systematic error in the temperature estimate is extremely unlikely. Since both copper and oxygen measurements show approximately the same temperature through the arc's transition the most logical conclusion is that self-absorption is negligible for both species for most points in the main transit of the arc with the exception of the initiation where the calculated temperatures of the two species do not match. The error bars in figure 10 are given by the standard deviation of normalized Boltzmann plotting method used. The low value of these error bars suggests that the RailPAc's temperature is a reproducible phenomenon since the method takes into account multiple firings. As with species concentration, no measurements were taken further down the rails because emission of the arc past this point suggests that the arc is not at LTE during the quench phase.

One might expect the variation in concentration of copper in the arc to have an effect on the temperature of the arc as discussed in [20]. However, since the methods used in that work could not resolve temperature changes through the arc and only captured an average temperature for the whole arc column, a variation in temperature of the level described in [20] would be smaller than the error bounds for the temperature measurements shown in figure 10. Our results show that the arc temperature remains relatively constant throughout the duration of the transient with very little sensitivity to the arc current. Other work in the literature corroborate our observation that for arc currents above ~200 A the arc temperature is only a relatively weak function of current [21–23], and [24].

## 4. Conclusion

The propagating arc of the RailPAc device was characterized with high-speed imaging, electrical measurements, and spectroscopy measurements. Three distinct stages of transit were observed. The initiation stage shows the formation and acceleration of a compact and coherent arc column. The arc column breaks into distinct bright anode and cathode columns connected by a less luminescent gas as the arc enters the main transit stage. The anode roots jump along the electrode during this stage, while the cathode roots move smoothly. These modes of transit result in a variety of repeatable fluctuations in current and breech voltage. In the quenching stage, the arc dissipates as the breech voltage drops below the minimum sustain voltage for the rail geometry.

The expansion of the arc column above the surface is a result of the combined effects of thermal expansion and induced magnetic fields on the columns. The differences in the characteristics of the anode root's motion in comparison to those of the cathode root were proven to result in more severe deformation of the anode electrode.

The RailPAc arc was found to have a temperature of ~10 000 K and variations in the relative concentrations of copper and oxygen species were detected. The high temperature of the arc and increasing content of copper species in the arc corroborate the ablation effects visible on the rail.

## Acknowledgments

This material is based upon work supported by, or in part by, the U.S. Army Research Laboratory and the U.S. Army Research Office under contract/grant number W911NF1410226.

## References

[1] Richard F, Cormier J M, Pellerin S and Chapelle J 1996 Physical study of a gliding arc discharge *J. Appl. Phys.* **79** 2245
[2] Pafford B, Sirohi J and Raja L L 2013 Propagating-arc magnetohydrodynamic plasma actuator for directional high-authority flow control in atmospheric air *J. Phys. D: Appl. Phys.* **46** 485208
[3] Parker J V 1989 Why plasma armature railguns don't work (and what can be done about it) *IEEE Trans. Magn.* **25** 418–24
[4] Yang F, Wu Y, Rong M, Sun H and Murphy A B 2013 Low-voltage circuit breaker arcs—simulation and measurements *J. Phys. D: Appl. Phys.* **46** 273001
[5] Ray P K 1989 Arc restrike in the rail accelerator *IEEE Trans. Magn.* **25** 485–8
[6] Koyama K, Toya H, Wada Y and Hasegawa A 1993 Arc behavior driven by electromagnetic force between rail electrodes *IEEE Trans. Magn.* **29** 843–7
[7] Laurent A, Mercier M and Velleaud G 1989 A study of the kinematics of a low-voltage breaking self-blown arc: Analysis of the derivative of the anode-cathode voltage *J. Phys. D: Appl. Phys.* **22** 933–40
[8] Zeller P R and Rieder W F 2001 Arc structure, arc motion, and gas pressure between laterally enclosed arc runners *IEEE Trans. Compon. Packag. Technol.* **24** 337–41
[9] Mercier M, Cajal D, Laurent A, Velleaud G and Gary F 1996 Evolution of a low-voltage electric arc *J. Phys. D: Appl. Phys.* **29** 95–8
[10] Teste P, Leblanc T and Chabrerie J P 1995 Study of the arc root displacement and 3D modelling of the thermal phenomena occuring in a hollow cathode submitted to an electric moving arc *J. Phys. D: Appl. Phys.* **28** 888–98

[11] Lindmayer M 1973 The influence of contact materials and chamber wall materials on the migration and the splitting of the arc in extinction chambers *IEEE Trans. Parts Hybrids Packag.* **9** 45–9
[12] Lindmayer M and Paulke J 1998 Arc motion and pressure formation in low voltage switchgear *IEEE Trans. Compon. Packag. Manuf. Technol.* A **21** 33–9
[13] Yi W and Rong M 2008 Numerical analysis of the effect of the chamber width and outlet area on the motion of an air arc plasma *IEEE Trans. Plasma Sci.* **36** 2831–7
[14] Weaver P M and McBride J W 1994 Magnetic and gas-dynamic effects on arc motion in miniature circuit-breakers *IEEE Trans. Compon. Packag. Manuf. Technol.* A **17** 39–46
[15] Kramida A, Ralchenko Y, Reader J and NIST 2014 *NIST Atomic Spectra Database (Ver. 5.2)*, [Online]. Available: http://physics.nist.gov/asd [25 February 2015] (Gaithersburg, MD: National Institute of Standards and Technology)
[16] Camacho J J 2007 Optical emission studies of nitrogen plasma generated by IR CO2 laser pulses *J. Phys. B: At. Mol. Opt. Phys.* **40** 4573–90
[17] Aguillera J A and Aragon C 2004 Characterization of a laser-induced plasma by spatially resolved spectroscopy of neutral atom and ion emissions. Comparison of local and spatially integrated measurements *Spectrochim. Acta* B **59** 1861–76
[18] Choi Y, Sirohi J and Raja L L 2015 Measurement of transient force produced by a propagating arc magnetohydrodynamic plasma actuator in quiescent atmospheric air *J. Phys. D: Appl. Phys.* **48** 425204
[19] Haug R, Hahn R, He Z J, Samba M and Gouloubi P C 1991 Current transfer between two parallel electrical arcs *J. Phys. D: Appl. Phys.* **24** 325–30
[20] Schnick M, Fussel U, Hertel M, Spille-Kohoff A and Murphy A B 2010 Metal vapour causes a central minimum in arc temperature in gas–metal arc welding through increased radiative emission *J. Phys. D: Appl. Phys.* **43** 022001
[21] Kowalenko V and Clark G A 2000 Temperature estimates for a railgun plasma armature *J. Phys. D: Appl. Phys.* **33** 230–41
[22] Zhu J, Gao J, Ehn A, Aldén M, Li Z, Moseev D, Kusano Y, Salewski M, Alpers A, Gritzmann P and Schwenk M 2015 Measurements of 3D slip velocities and plasma column lengths of a gliding arc discharge *Appl. Phys. Lett.* **106** 044101
[23] Ma R, Rong M, Yang F, Wu Y, Sun H, Yuan D, Wang H and Niu C 2013 Investigation on arc behavior during arc motion in air dc circuit breaker *IEEE Trans. Plasma Sci.* **41** 2551–60
[24] Glickstein S S 1976 Temperature measurements in a free burning arc *Weld. Res. Suppl.* **1976** 222–9